Electronic Supplementary Information (ESI)

Conducting Polymer Transforms Hydrophobic Porous Membranes into Robust Gas Diffusion Layers in Electrochemical Applications

Hwiyoon Noh[1], Hyunki Yeo[1], Bryan W. Boudouris[1,*], and Brian M. Tackett[1,*]

[1] Charles D. Davidson School of Chemical Engineering, Purdue University, West Lafayette, IN 47907, United States

* Corresponding author: Bryan W. Boudouris and Brian M. Tackett

E-mail address: boudouris@purdue.edu, Tel: +1-765-496-6056, and Fax: +1-765-494-0805

E-mail address: bmtacket@purdue.edu, Tel: +1-765-496-7235, and Fax: +1-765-494-0805

Details in spectroscopic analysis of PEDOT-PTFE

In Raman spectra (Fig. 2a), PTFE showed 6 distinguished bands at 288, 383, 730, 1155, 1299, and 1327 cm^{-1}. Specifically, the first band at 288 cm^{-1} is the superposition of the CF_2 bond and the band at 383 cm^{-1} originates from the CF_2 deformation. The symmetric and asymmetric stretching of CF_2 bonds is associated with the bands at 730 and 1155 cm^{-1}. The last two bands (1299 and 1327 cm^{-1}) are assigned to the stretching of C-C bonds. All of the bands showed a good agreement with previous literature, meaning the structural integrity of PTFE.[1,2] For PEDOT-PTFE, distinguished characteristic bands indicate the successful formation of PEDOT on the PTFE membrane. Specifically, three bands at 438, 576, and 988 cm^{-1} are associated with the oxyethylene ring deformation.[3] Additionally, one band at 696 cm^{-1} shows the deformation of the C – S – C bond while two bands at 853 and 1130 cm^{-1} stem from the C – O – C bond deformation.[4–6] Moreover, the bands at 1256 and 1367 cm^{-1} represent the $C_\alpha – C_\alpha$ and $C_\beta – C_\beta$ stretching, respectively. Two bands near 1430 cm^{-1} are attributed to symmetric $C_\alpha = C_\beta$ stretching whereas two bands at 1528 and 1560 cm^{-1} are due to asymmetric $C_\alpha = C_\beta$ stretching, meaning the formation of PEDOT through electropolymerization.[7] Relatively small bands not included in PEDOT are observed at 288, 383, and 730 cm^{-1} and overlapped with the PTFE spectrum, indicating these bands originates from PTFE. Thus, it is worth noting that the monomer, EDOT, was successfully oxidized on the Au-coated PTFE and underwent radical polymerization forming PEDOT.

FTIR spectrum of PEDOT-PTFE shown in Fig. 2b is the additional proof of the formation of the PEDOT layer on the PTFE membrane. In detail, two peaks (856 and 935 cm^{-1}) are related to the stretching vibration of C – S in thiophene ring, three peaks (1062, 1122, and 1164 cm^{-1}) originate from the stretching of C – O – C in dioxyethylene ring, two peaks (1390 and 1463 cm^{-1}) are associated with C – C bond stretching in the ring, and the peak at 1583 cm^{-1} corresponds to the stretching of C = C bond in the ring in accordance with previous works.[8,9] The other unmarked two peaks at 989 and 1271 cm^{-1} are induced from dopant (in here, PF_6^-).[9] Interestingly, PTFE peaks at 1203 and 1149 cm^{-1} shown in the inset of Fig. 2b were not shown in the spectrum of PEDOT-PTFE meaning the surface of PTFE was well-covered by the PEDOT

layer. Both Raman and FTIR spectra confirmed the successful formation of the thin PEDOT layer on the PTFE membrane and its structural integrity even after undergoing aqua regia treatment.

To determine chemical states of each component in detail, high-resolution XPS spectra were further obtained in Fig. S8 and S9 and quantification result with peak assignation is in Table S1. Specifically, three in peaks are observed in C 1s, C – S at 284.8 eV, C = C – O at 286.2 eV, and O – C – O at 287.2 eV and these are conventional C 1s peaks appeared in electrochemically synthesized PEDOT structure.[10] The other peak centered at 289.1 eV can be attributed to overoxidation of monomer, possibly induced from electropolymerization process or aqua regia treatment. In S 2p, peaks are deconvoluted in two distinguished peaks: C – S – C in thiophene ring at 163.7 and 164.9 eV, and broad peaks originated from the same feature in positively charged PEDOT at 165.4 and 166.6 eV.[10–12] The O 1s spectrum shows main peak at 533.2 eV corresponding to oxygen species in dioxyethylene ring and other two peaks can be associated with shake-up peak or carboxyl/carbonyl group from overoxidation.[10,13] For N 1s, a peak centered at 400.2 eV was observed. This peak can be originated from either nitrile from the solvent used in the electropolymerization or nitrogen insertion in the carbon ring of PEDOT. Considering the reactivity of nitrile with acid, it is less likely derived from the solvent. Thus, the small percentage of N species were likely introduced into PEDOT structure, especially in thiophene ring, during the electropolymerization process due to minor overoxidation of PEDOT, which has been observed previously.[14] Due to the presence of PF_6^-, broad P 2p peaks at 135.9 and 136.8 eV were measured. Two F 1s peaks, centered at 686.4 and 690.1 eV, were identified and are attributed to PF_6^- and PTFE, respectively.

Fig. S9 depicts the change of high-resolution XPS spectra of Au 4f and Cl 2p before and after the aqua regia treatment. Prior to the treatment, none of Au and Cl species were observed. In contrast, after the treatment, both Au and Cl were identified. For Cl, this result is in good alignment with the EDX results in Fig. S7. Thus, Cl species were introduced to the PEDOT layer during the aqua regia treatment. As opposed to Cl, a substantial amount of Au was measured before the treatment in Fig. S7, distinct from the high-resolution XPS results in Fig. S9. It was found that the PEDOT layer fully covered the PTFE membrane

through microscopic and spectroscopic analysis. On top of that, XPS is surface-sensitive characterization whereas EDX is a bulk technique. Considering these factors, and that Au species were only measurable in XPS after the aqua regia treatment, it is believed that small amounts of Au become incorporated in the PEDOT structure during the aqua regia treatment. Furthermore, as shown in Fig. S5, the treatment-induced change in electrical conductivity is marginal since the dominant dopant was still PF_6^- even after the treatment (Table S1). In Au 4f, two oxidation states are observed – metallic Au (84.3 and 88.0 eV) and Au^{3+} (85.7 and 89.4 eV).[15–17] Two different states of chlorine, organic chlorine at 200.5 and 202.1 eV and chlorine ion at 196.8 and 198.4 eV, were observed in Cl 2p region.[18] The majority of chlorine corresponded to organic chlorine, indicating chlorination of PEDOT after the treatment. Considering the results of both Au 4f and Cl 2p spectra, a small portion of chlorine is likely to be combined with Au^{3+}, forming gold chloride species such as $AuCl_4^-$. Therefore, the aqua regia treatment resulted in Cl introduction as well as migration and insertion of Au species into PEDOT structure.

CO2RR performance of bare PEDOT-PTFE

The tests using bare PEDOT-PTFE without catalyst loading were carried out (Fig. S11). Even though the high potential was applied to PEDOT-PTFE (i.e. –2.0 V vs. RHE, for convenience, V represents V vs. RHE), the corresponding current density was negligible for all electrolytes. In detail, the current density reached to ca. –2.0 mA·cm^{-2} at –1.0 V and ca. –8.0 mA·cm^{-2} at –2.0 V in the alkaline electrolyte. In contrast, the current densities in neutral and acidic electrolytes were much lower than those in the alkaline electrolyte. The measured current density was ca. –0.6 mA·cm^{-2} at –1.0 V and ca. –3.0 mA·cm^{-2} at –2.0 V in the neutral medium whereas that was ca. –0.6 mA·cm^{-2} at –1.0 V and ca. –1.2 mA·cm^{-2} at –2.0 V in the acidic electrolyte. Otherwise, for example, PEDOT-PTFE with Ag nanopowder (NP) required –0.9 V (alkaline), –1.6 V (neutral), and –1.8 V (acidic) to obtain total current density of –200 mA·cm^{-2} (Fig. 3). Considering the results of bare PEDOT-PTFE at corresponding potential, less than 1% of products originated from PEDOT or residual Au species. For all current densities shown in Fig. 3, this negligible contribution was observed as well. Based on the results, the possibilities that PEDOT itself and the

remaining metallic Au species can actively participate in CO2RR were ruled out. In addition, it can be assumed that all products solely come from the CO2RR of Ag NPs.

Results of stability tests of PEDOT-PTFE and Sigracet 22bb

For the sake of reproducibility, total three repeats for each GDL under each electrolyte at a certain current density were performed and shown in Fig. S12 and S13. It is noteworthy that though the deviations among samples led to variation in CO faradaic efficiency and the initiation of electrolyte flooding, samples under a certain condition exhibited similar behavior, solidifying the excellence of PEDOT-PTFE. For instance, Sigracet 22bb under neutral electrolyte at -100 mA·cm^{-2} obviously indicated continuous electrolyte flooding proven by decrease in CO faradaic efficiency and oscillation in CO_2 flow rate (Fig. S12b1 and b2) although the steepness in the decrease and the time when oscillation started varied in each sample. In contrast, the counterpart, PEDOT-PTFE, did not suffer from electrolyte flooding, proven by stable CO_2 flow rate (Fig. S12b3), and sustain its initial catalytic performance without precipitous or gradual CO faradaic efficiency decrease (Fig. S12b1). Likewise, the same was observed for all other cases. Furthermore, all results from PEDOT-PTFE at each condition exceeded CO faradaic efficiency from Sigracet 22bb even for longer operation regardless of the identify of electrolyte and the intensity of current density. Thus, it is obvious that PEDOT-PTFE has substantially enhanced flooding resistance compared to carbon-based GDL, resulting in the improved preservation of its original catalytic activity. Trial 1 in each case in Fig. S12 and S13 was used as a representative in Fig. 4, and details including potential, CO_2 flow rate with CO and H_2 faradaic efficiencies as well as the total faradaic efficiency are provided in Fig. S14-16 and discussed further in following.

Under alkaline environment (0.8 M KOH), CO faradaic efficiency started to decrease as time goes for the case of Sigracet 22bb regardless of the current density. In addition, the deactivation rate was similar between -100 and -200 mA·cm^{-2}; after 12 h operation, CO faradaic efficiency was diminished to 58.4% at -100 mA·cm^{-2} and to 59.0% at -200 mA·cm^{-2}. Continuous oscillation in CO_2 mass flow was not observed in the alkaline electrolyte for both current densities (Fig. S14a1 and S14b1), indicating severe electrolyte

flooding was less likely to occur. Furthermore, the sum of faradaic efficiency was maintained for the operation period, but the selectivity production of CO was altered to H_2 as shown in Fig. S14a2 and S14b2. On the other hand, although marginal decrease in CO faradaic efficiency along with the increase of operation time was observed, PEDOT-PTFE showed higher durability to sustain the efficiency for extended time for both current densities compared to Sigracet 22bb in the alkaline condition (Fig. 4 and S14). Specifically, under constant -100 mA·cm^{-2}, CO faradaic efficiency started from 97.4% and decreased to 96.6% after 12 h and 93.9% after 20 h. Under -200 mA·cm^{-2}, the efficiency decreased from 91.8% to 91.0% after 12 h and 90.0% after 20 h. These results are much higher than the results of Sigracet 22bb, indicating the excellence of PEDOT-PTFE for long-term operation as gas diffusion layer (GDL). In a similar way to Sigracet 22bb, continuous electrolyte flooding was not observed as well in PEDOT-PTFE whereas minor fluctuation in CO_2 flow rate was observed possibly due to pressure change induced by sample injection (Fig. S14c1 and S14d1). Moreover, the sum of faradaic efficiency persisted as well for both -100 and -200 mA·cm^{-2} and PEDOT-PTFE maintained the selectivity toward CO much effectively compared to Sigracet 22bb (Fig. S14c2 and S14d2). As the operation started, the CO faradaic efficiency of Sigracet 22bb decreased fast and selective H_2 production was triggered to same extent in both current densities. However, the increase in H_2 faradaic efficiency was remarkably mitigated in the case of PEDOT-PTFE while maintaining CO faradaic efficiency. Consequently, PEDOT-PTFE with Ag NPs was able to successfully maintain selective production of CO for extended time compared to Sigracet 22bb for both current densities under the alkaline condition.

The stability tests using the neutral electrolyte (0.8 M KHCO$_3$) showed a different trend compared to the alkaline case, but they also showed the enhanced durability of PEDOT-PTFE than Sigracet 22bb. In details, Sigracet 22bb kept CO faradaic efficiency to some extent until 16 h at -100 mA·cm^{-2}, and the efficiency started to decrease and reach to 79.4% at 20 h (Fig. 4a and S15a2). At constant -200 mA·cm^{-2}, steep decrease in CO faradaic efficiency was suddenly observed at 7.5 h, finally falling to 47% at 8 h (Fig. 4c and S15b2). There was a significant oscillation in the CO_2 mass flow rate indicating severe electrolyte

flooding at constant -100 mA·cm^{-2} after 16 h (Fig. 4b and S15a1). Typically, a decrease in product faradaic efficiency is accompanied by continuous electrolyte flooding, due to the blockage of CO_2 transport by flooded electrolyte.[19,20] This phenomenon was also observed in Sigracet 22bb; a continuous decrease of CO faradaic efficiency with the oscillation in the flow rate clearly indicates severe electrolyte flooding took place in the case of Sigracet 22bb. At the same time, the increase in H_2 faradaic efficiency was also observed, indicating stimulation of H_2 production caused by lack of gas reactant, CO_2, with the fact that the sum of faradaic efficiencies became to be diminished slightly (Fig. S15a2). Under -200 mA·cm^{-2}, the continuous electrolyte flooding occurred at an early stage, 7.5 h, for Sigracet 22bb (Fig. 4d and S15b1). Whereas the increase in H_2 faradaic efficiency and decrease in the sum of faradaic efficiency was less prominent at -100 mA·cm^{-2}, stark increase in H_2 production and loss in GDL ability was clearly observed at -200 mA·cm^{-2} (Fig. S15b2). Compared to Sigracet 22bb, PEDOT-PTFE sustained CO faradaic efficiency until 20 h operation for both current densities without significant loss (Fig. 4, S15c2, and S15d2). At -100 mA·cm^{-2}, it is clearly observed that CO faradaic efficiency from Sigracet 22bb starts to decrease at 16 h and the faradaic efficiency from PEDOT-PTFE finally exceeds the result from Sigracet 22bb around 20 h. Interestingly, at -200 mA·cm^{-2}, remarkable enhancement in the stability of PEDOT-PTFE as GDL can be found as, unlike Sigracet 22bb, sudden decrease in CO faradaic efficiency was not observed. None of the oscillation in the CO_2 flow rate was observed in PEDOT-PTFE except for small disturbance caused by the GC injection regardless of current densities, meaning the stability for maintaining CO2RR performance was stem from the ability of GDL preventing the severe electrolyte flooding (Fig. 4 and S15c1, S15d1). In terms of GDL performance, for both current densities, the sum of faradaic efficiencies was almost constant, showing PEDOT-PTFE can maintain its GDL ability for much longer time compared to Sigracet 22bb (Fig. S15c2 and S15d2). Thus, PEDOT-PTFE has much higher resistance to continuous electrolyte flooding, leading to enhanced stability for long-term CO2RR operation under the neutral electrolyte.

For stability tests in the acidic electrolyte (0.01 M H_2SO_4 with 0.4 M K_2SO_4), a steep decrease in CO faradaic efficiency at -200 mA·cm^{-2} was observed at 4.5 h for the case of Sigracet 22bb, while the

deactivation was slightly diminished until 12 h and accelerated after 12 h at -100 mA·cm^{-2} (Fig. 4, S16a2, and S16b2). In contrast, the sluggish decrease was found for PEDOT-PTFE at -100 mA·cm^{-2} compared to Sigracet 22bb (Fig. 4 and S16c2). Moreover, instead steep decrease in early period like Sigracet 22bb, monotonic decrease in CO faradaic efficiency with time was observed at -200 mA·cm^{-2} (Fig. 4 and S16d2). This result is in good agreement with the result in the neutral electrolyte, higher current leads to prominent decrease in CO faradaic efficiency. However, whereas PEDOT-PTFE maintained the efficiency until 20 h operation in the neutral electrolyte, PEDOT-PTFE showed continuous decrease in the efficiency even though it was much better than Sigracet 22bb. For constant -100 mA·cm^{-2} of Sigracet 22bb, severe electrolyte flooding was observed due to moderate oscillation in CO_2 flow rate with decrease CO faradaic efficiency (Fig. S16a1). On the other hand, like the neutral electrolyte, large noise in CO_2 flow rate was observed starting from 4.5 h and severe electrolyte flooding caused the steep decrease in CO faradaic efficiency at -200 mA·cm^{-2} (Fig. S16b1). This is further identified by changes in faradaic efficiencies (Fig. S16a2 and S16b2). While the sum of faradaic efficiencies at -100 mA·cm^{-2} was almost constant, it started to decrease at 4.5 h with the increase of H_2 faradaic efficiency at -200 mA·cm^{-2}, demonstrating diffusion blockage of both reactant and product caused by electrolyte flooding. In contrast, PEDOT-PTFE did not suffer from severe electrolyte flooding issue under the acidic environment since continuous fluctuation in CO_2 flow rate was not present (Fig. S16c1 and S16d1). In contrast, the sum of faradaic efficiency was maintained in the case of -100 mA·cm^{-2}, but it slightly decreased with the time for -200 mA·cm^{-2} case (Fig. S16c2 and S16d2). Overall, even though decrease in CO2RR activity was observed for both Sigracet 22bb and PEDOT-PTFE, PEDOT-PTFE did not suffer from electrolyte flooding, resulting in enhanced stability as GDL compared to Sigracet 22bb.
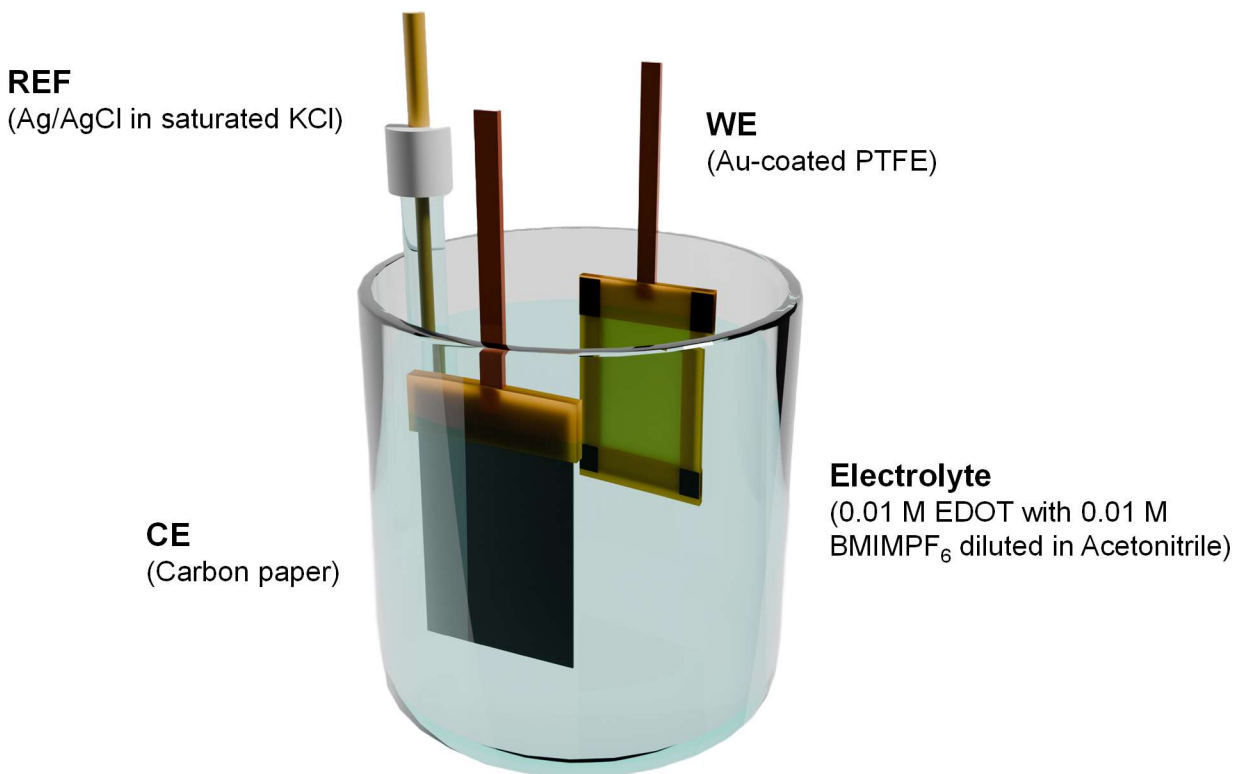
Fig. S20 shows the stability test of AgNP loaded PEDOT-PTFE for extended period (81 h). Missing data points at ~45 h in Fig. S20 are a result of GC software malfunction that did not affect reactor performance. Data collection resumed after the software was restarted. Until 20 h, it well maintained its performance with minute decrease in CO faradaic efficiency. However, it started to decrease and reached

80.3% at 24 h, 74.9% at 48 h, 67.1% at 72 h, and 64.3% at 81 h. The calculated decline rate of faradaic efficiencies for CO, H_2, and sum of faradaic efficiencies were –0.27, +0.05, and –0.22 %·hr^{-1}, respectively. Despite the decrease of product selectivity, the CO_2 flowrate did not show any distinguished feature of severe electrolyte flooding within the reaction period. In order to figure out the cause for decrease of CO faradaic efficiency, the comparison between pristine and used AgNP on PEDOT-PTFE was performed using SEM/EDX and shown in Fig. S21. The SEM image after the test clearly showed the catalyst detachment as the GDL surface is exposed whereas pristine showed a well-covered catalyst layer (Fig. S21a and S21c). In addition, pristine electrode did not show any K species in EDX spectrum (Fig. S21b). After the stability test, the amount of K species drastically increased indicating the presence of K species in the used electrode (Fig. S21d). Considering the decrease in CO faradaic efficiency and total faradaic efficiency with the increase in H_2 faradaic efficiency, both catalyst detachment and a decrease in gas diffusion ability caused by salt precipitation simultaneously occurred during the test, resulting in the trend shown in Fig. S20. However, it is clear that PEDOT-PTFE didn't show any characteristics of electrolyte flooding, which is opposed to the case of Sigracet 22bb.
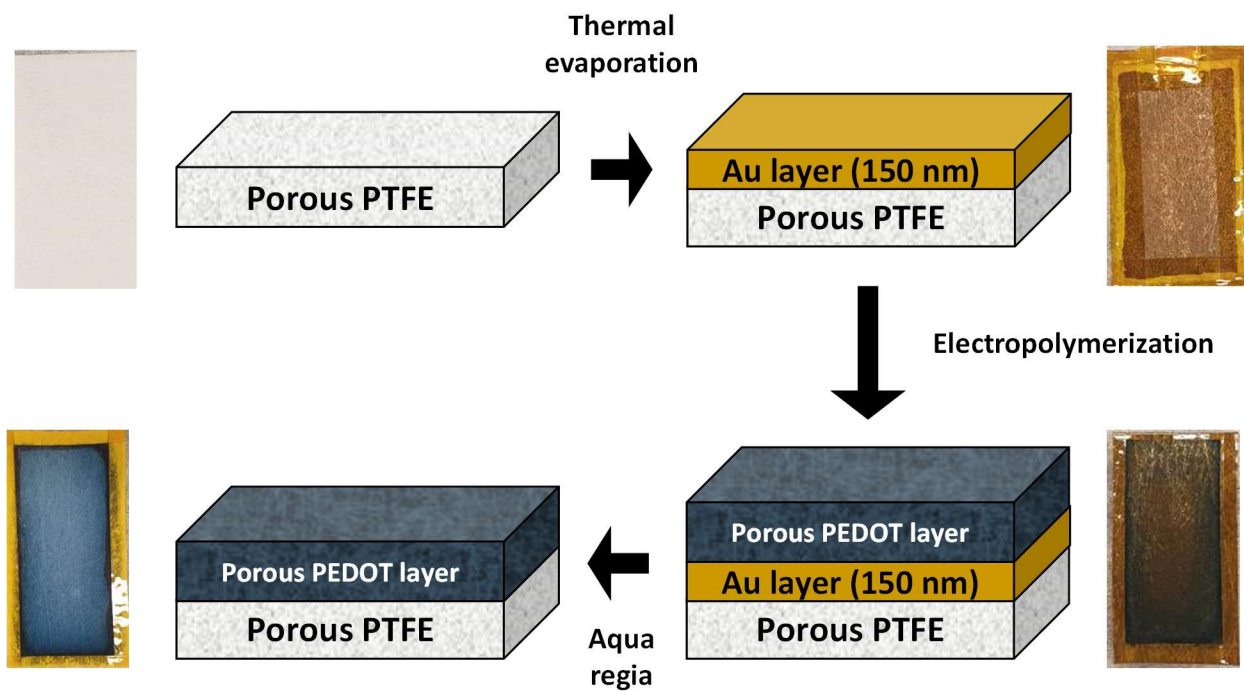
Fig. S1 Scheme of PEDOT-PTFE production. Image of PTFE membrane at each stage is shown next to the scheme of PTFE structure.

REF
(Ag/AgCl in saturated KCl)

WE
(Au-coated PTFE)

CE
(Carbon paper)

Electrolyte
(0.01 M EDOT with 0.01 M
BMIMPF$_6$ diluted in Acetonitrile)

Fig. S2 Cell setup for electrochemical synthesis of PEDOT on PTFE membrane. For electropolymerization, three-electrode configuration was used: working electrode (WE, Au-coated PTFE), counter electrode (CE, carbon paper), and reference electrode (REF, Ag/AgCl in saturated KCl). For electrolyte, 100 mL of acetonitrile containing 0.01 M of 3,4-ethylenedioxythiophene (EDOT) and 0.01 M of 1-butyl-3-methylimidazolium hexafluorophosphate (BMIMPF$_6$) was used. To prevent concentration change, top part of the cell was tightly covered by parafilm.
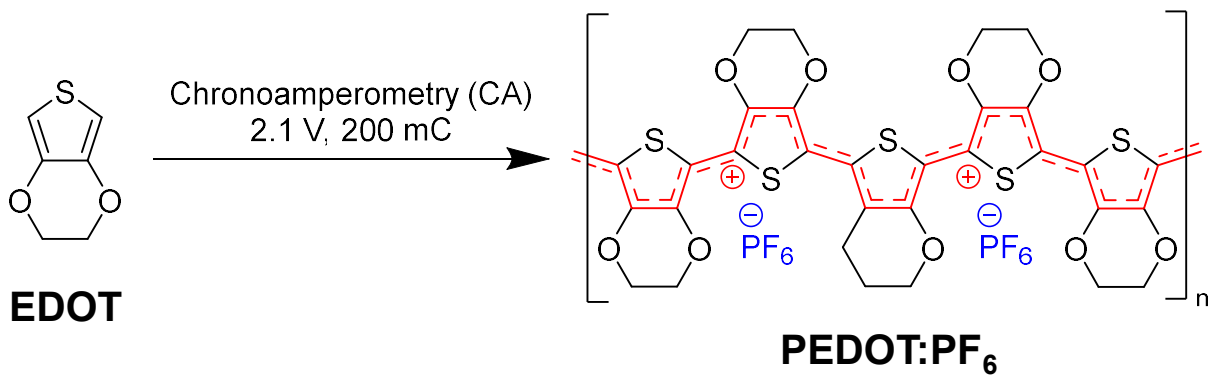
Fig. S3 Chemical equation of electropolymerization of EDOT to PEDOT:PF$_6$.
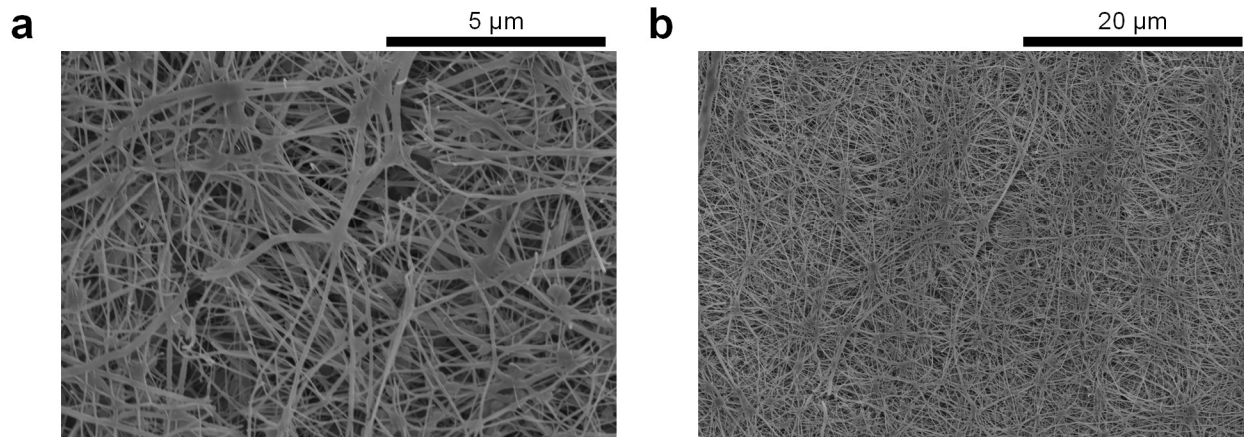
Fig. S4 SEM image of PTFE membrane at (a) high magnification and (b) low magnification.
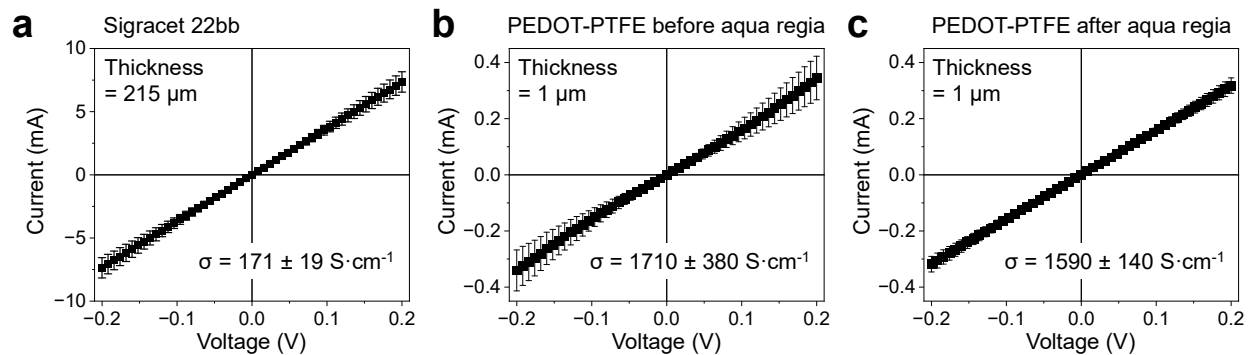
Fig. S5 I-V curve of (a) Sigracet 22bb, PEDOT-PTFE (b) before and (c) after aqua regia treatment and calculated electrical conductivity. The average and standard deviation were obtained from 9 independent samples.
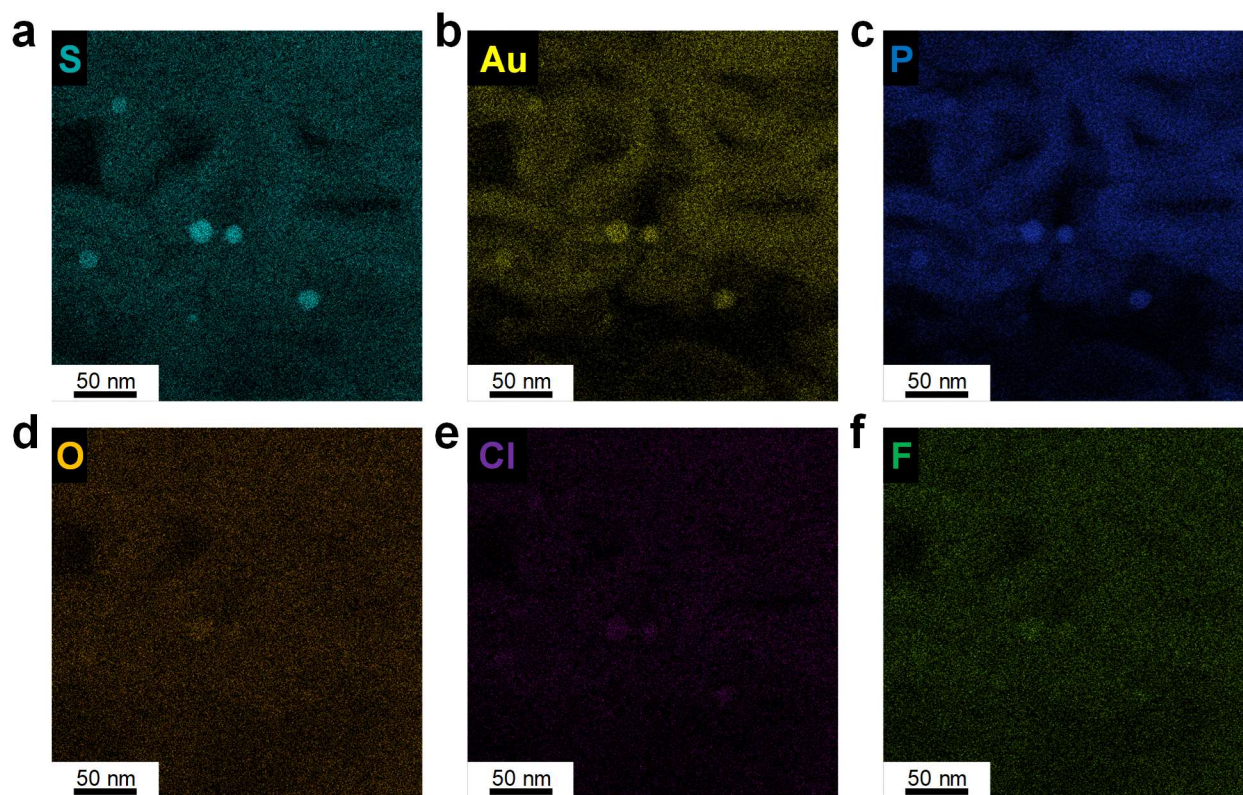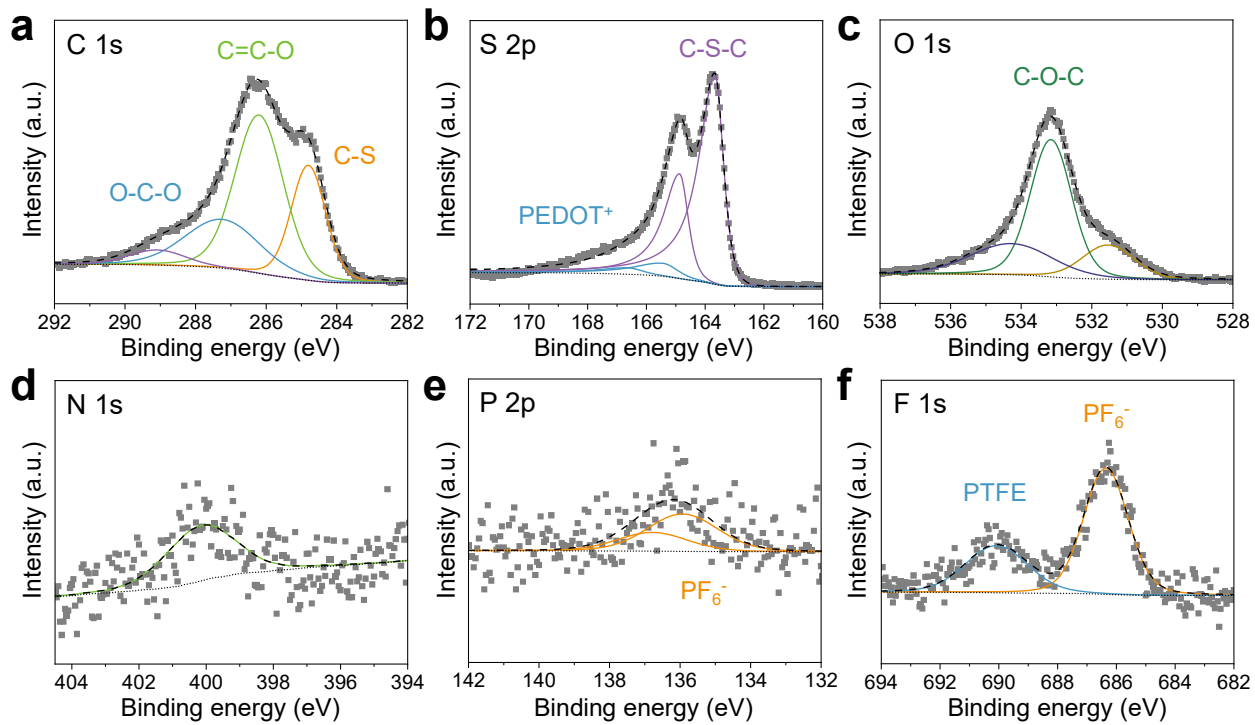
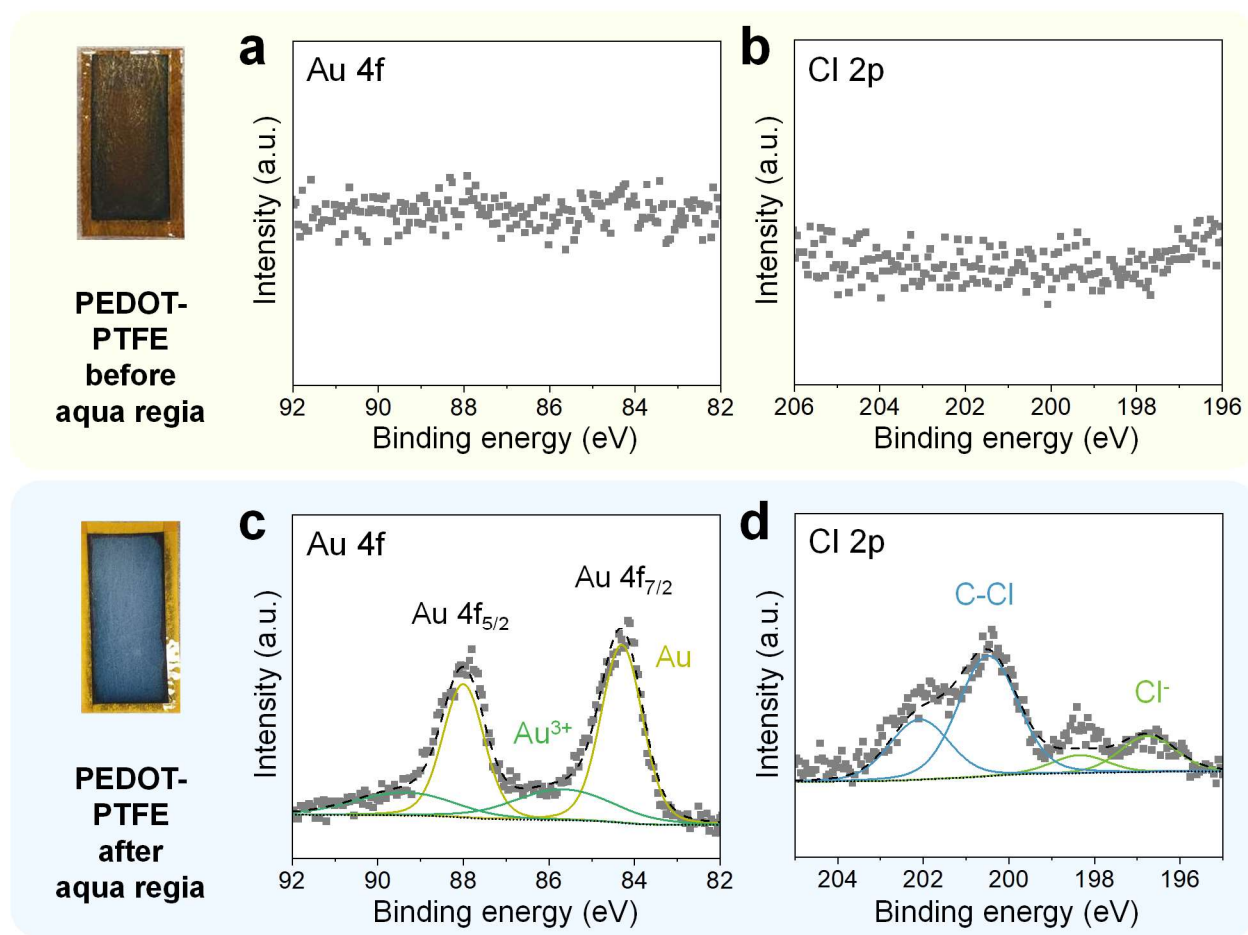**Fig. S6** EDX mapping images of (a) S, (b) Au, (c) P, (d) O, (e) Cl, and (f) F from HAADF-STEM image.
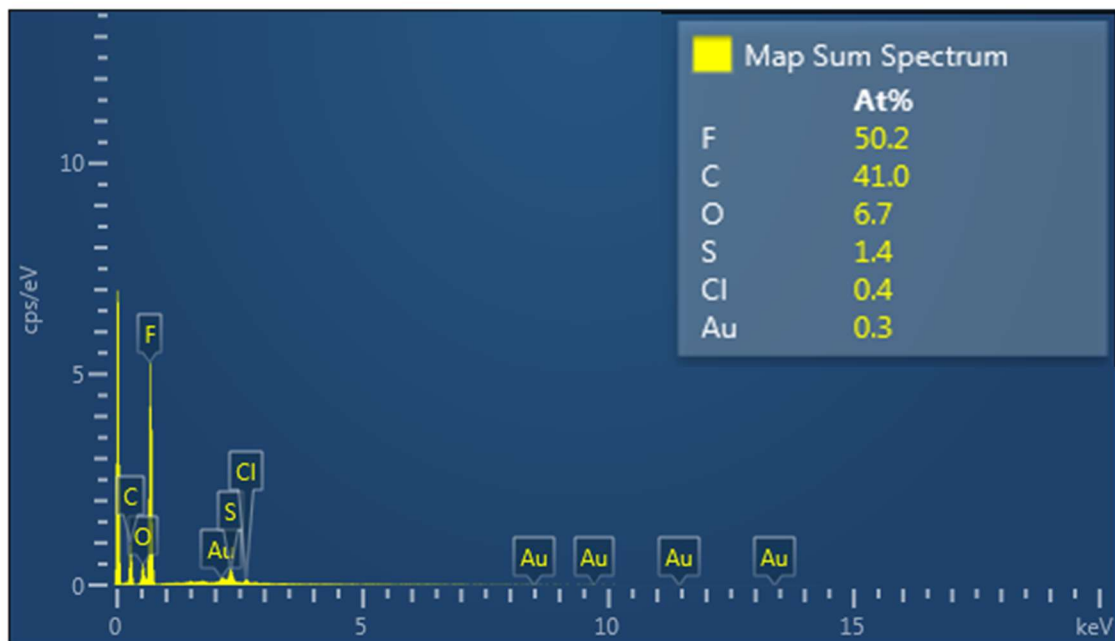
Fig. S7 EDX spectra of (a) PEDOT-PTFE before aqua regia treatment and (b) PEDOT-PTFE after aqua regia treatment. The area used for these spectra was 120×120 μm^2 using 1k× magnification.

**Fig. S8** High-resolution XPS spectra of (a) C 1s, (b) S 2p, (c) O 1s, (d) N 1s, (e) P 2p, and (f) F 1s.

Fig. S9 High-resolution XPS spectra of (a, c) Au 4f and (b, d) Cl 2p of PEDOT-PTFE (a, b) before and (c, d) after aqua regia treatment.

**Table S1** Quantification of XPS results

| Species	Assignment	Binding Energy (eV)	At%
C 1s	C-S	284.8	15.29
	C=C-O	286.2	29.42
	C-O-C	287.2	14.07
	Overoxidized C	289.1	3.28
S 2p	C-S-C	163.7, 164.9	8.14
	PEDOT$^+$	165.4, 166.6	0.89
O 1s	Carboxyl/Carbonyl	531.5	4.66
	C-O-C	533.2	14.87
	Shake-up	534.3	6.70
Au 4f	Au	84.3, 88.0	0.09
	Au^{3+}	85.7, 89.4	0.04
Cl 2p	Cl$^-$	196.8, 198.4	0.23
	C-Cl	200.5, 202.1	0.83
F 1s	PF$_6^-$	686.4	0.68
	PTFE	690.1	0.36
P 2p	PF$_6^-$	135.9, 136.8	0.17
N 1s	N species in PEDOT	400.2	0.28
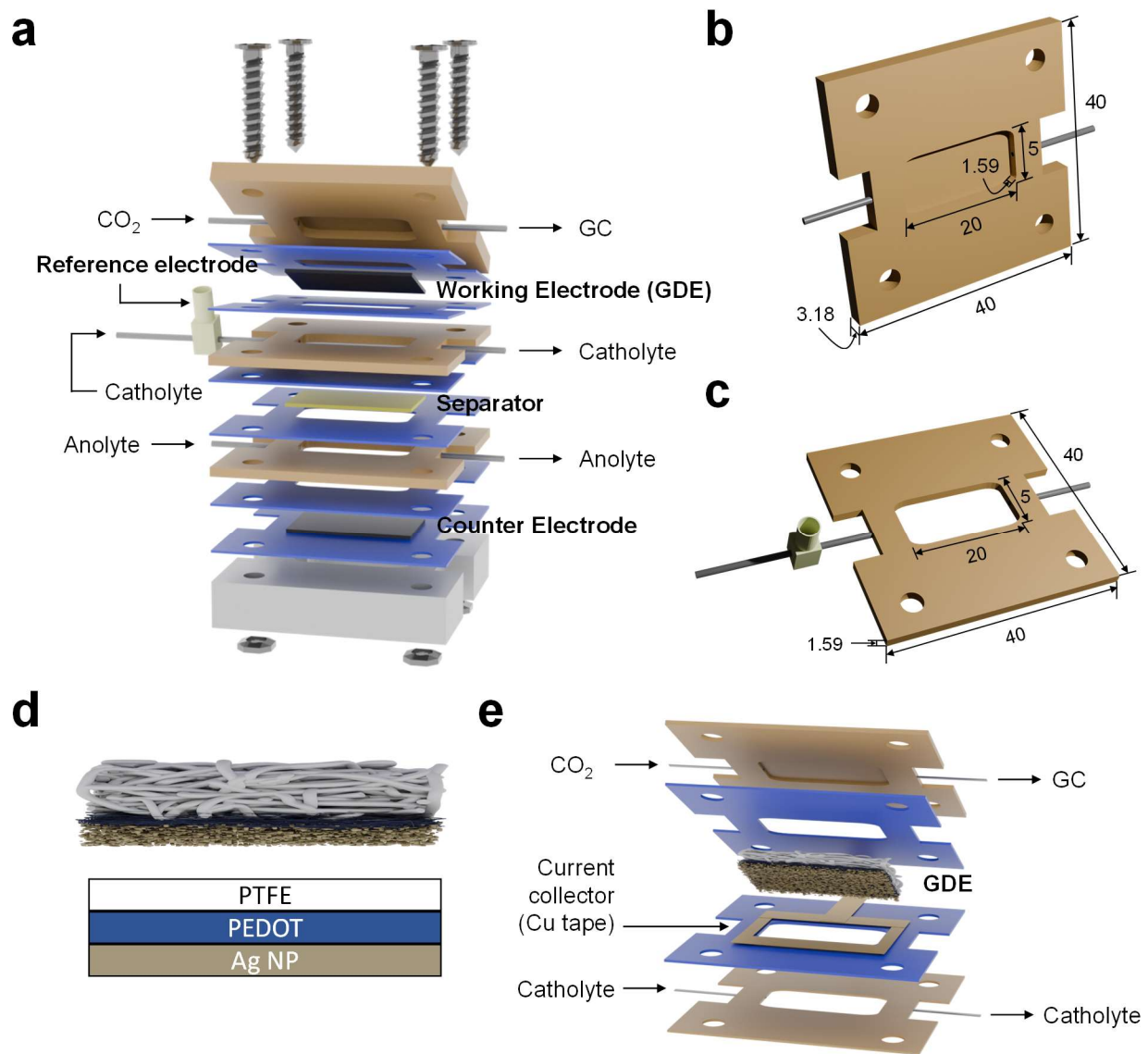
Fig. S10 Schematics of the lab-made flow cell. (a) Entire assembly of the flow cell with three-electrode configuration. Specific dimensions of (b) gas channel and (c) liquid channel. The numbers shown in (b) and (c) have the unit of millimeter (mm). The thickness of gas and liquid channels is 1.59 mm and the exposed area for each electrode is 1cm². Gas and liquid channels are made by polyether ether ketone (PEEK) and stainless steel is used for the bottom part in (a). (d) Schematic illustration of catalyst (in here, 1.0 mg·cm⁻² of Ag NP) loaded PEDOT-PTFE. (e) Catalyst-loaded PEDOT-PTFE (working electrode) assembly with front contacting using Cu tape as a current collector.
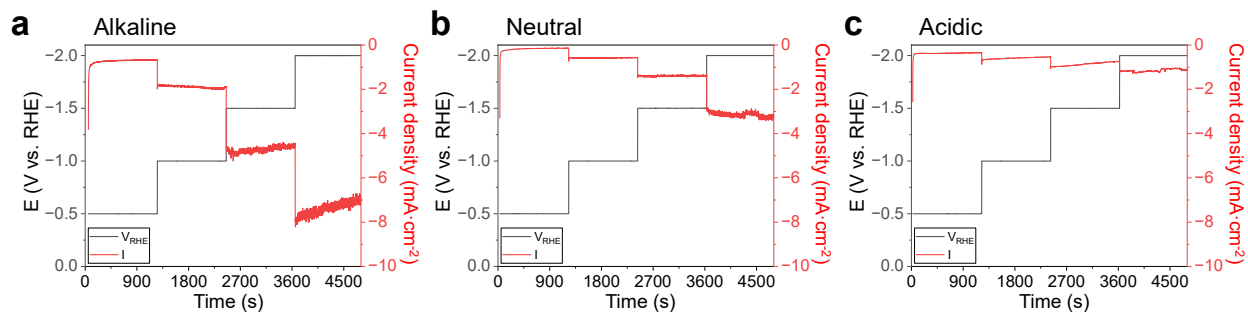
Fig. S11 CO2RR test of bare PEDOT-PTFE without catalyst loading in (a) alkaline (0.8 M KOH), (b) neutral (0.8 M KHCO$_3$), and (c) acidic (0.01 M H$_2$SO$_4$ with 0.4 M K$_2$SO$_4$) electrolytes. Chronoamperometry was used for this measurement. Each potential step from –0.5 V vs. RHE to –2.0 V vs. RHE with the increment of –0.5 V vs. RHE was applied for 20 min. Gas and electrolyte flow rates followed the same experimental conditions in the method section.
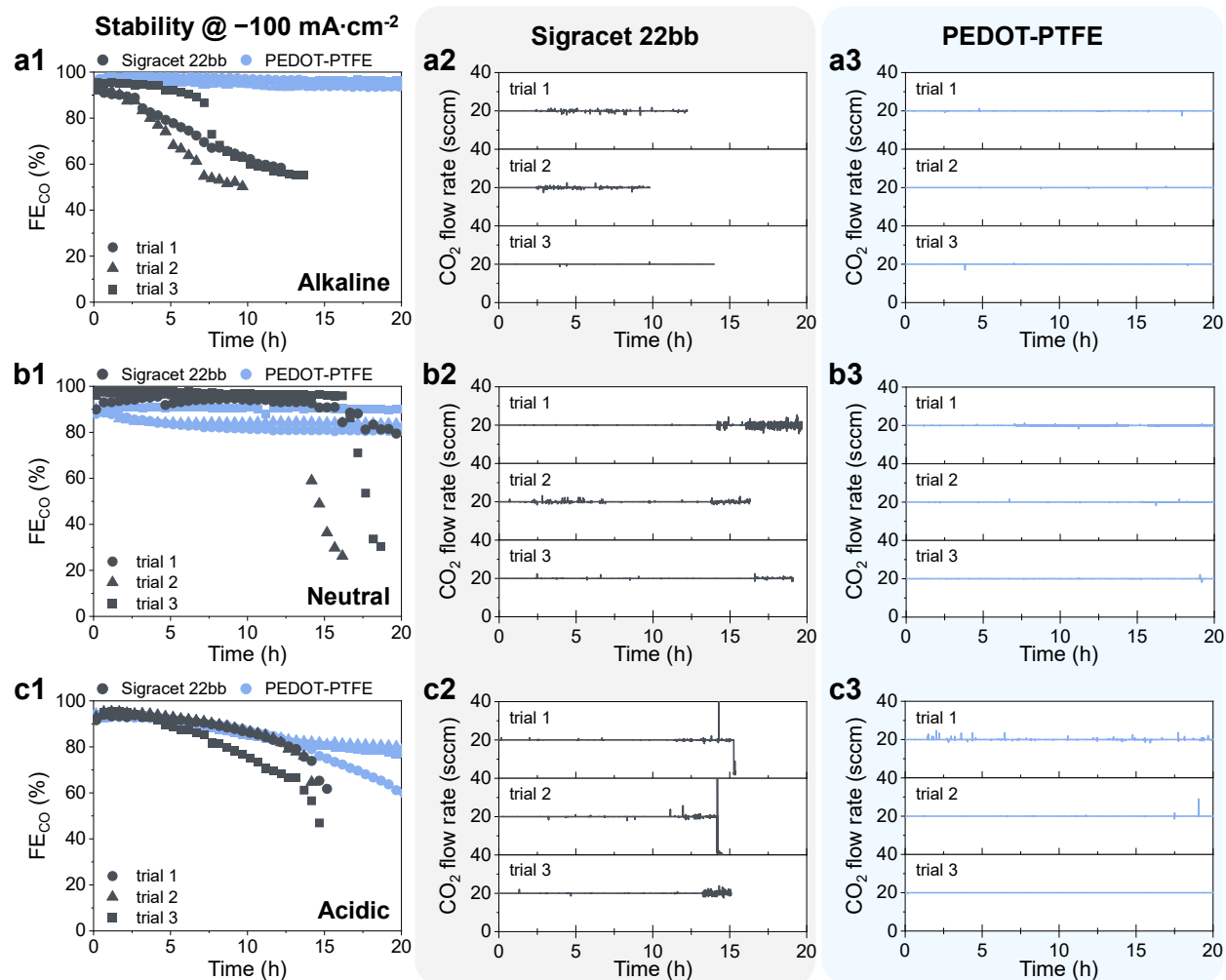
Fig. S12 Stability tests at −100 mA·cm^{-2} in (a) alkaline (0.8 M KOH), (b) neutral (0.8 M KHCO$_3$), and (c) acidic (0.01 M H$_2$SO$_4$ with 0.4 M K$_2$SO$_4$) electrolytes. (a1-c1) CO faradaic efficiency calculated from GC and CO$_2$ flow rate recorded by MFC from (a2-c2) Sigracet 22bb and (a3-c3) PEDOT-PTFE along with reaction time. In (a1-c1), circle, triangle, and square indicate independent experiments. In this figure, black and blue stand for Sigracet 22bb and PEDOT-PTFE, respectively.
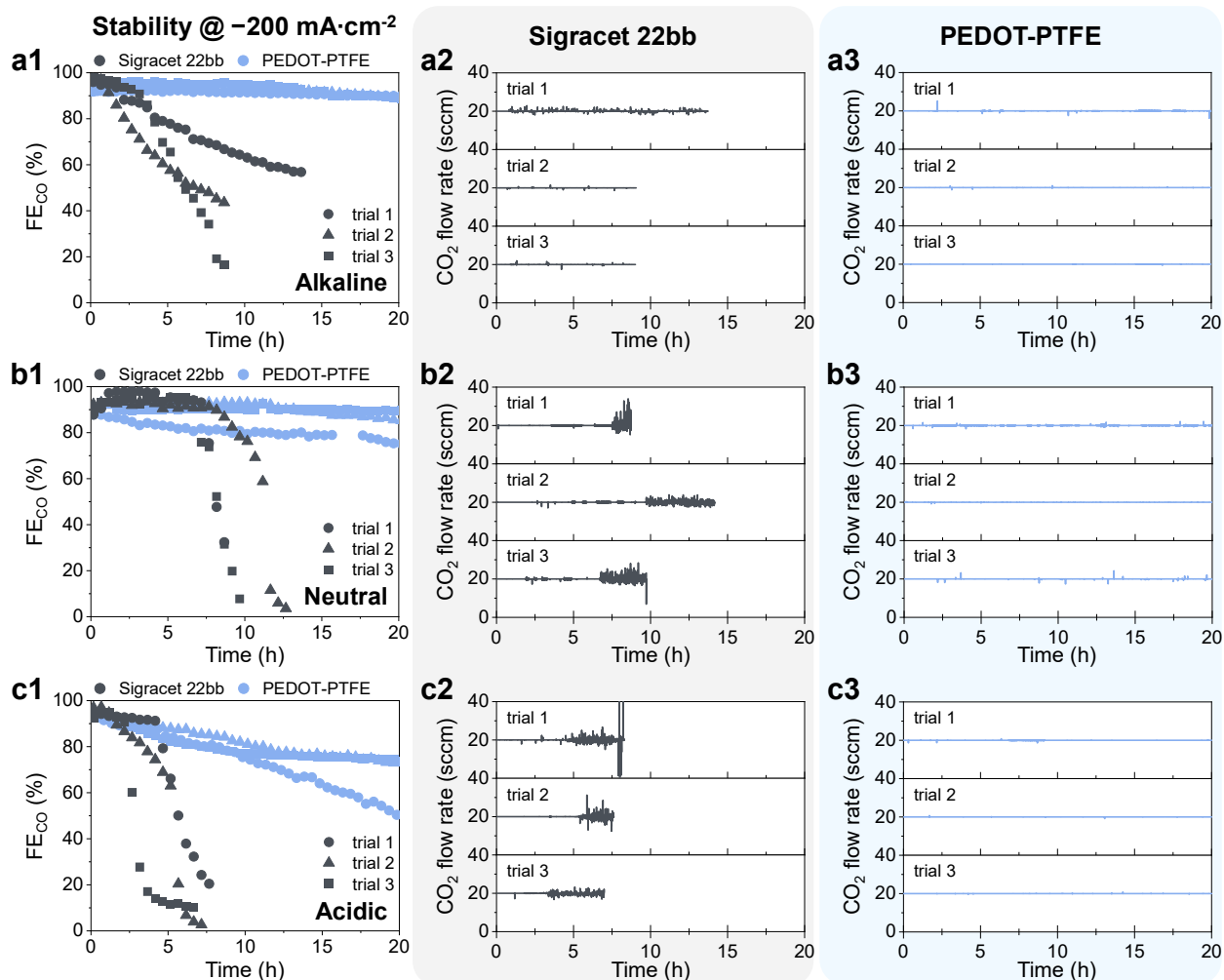
Fig. S13 Stability tests at −200 mA·cm^{-2} in (a) alkaline (0.8 M KOH), (b) neutral (0.8 M KHCO$_3$), and (c) acidic (0.01 M H$_2$SO$_4$ with 0.4 M K$_2$SO$_4$) electrolytes. (a1-c1) CO faradaic efficiency calculated from GC and CO$_2$ flow rate recorded by MFC from (a2-c2) Sigracet 22bb and (a3-c3) PEDOT-PTFE along with reaction time. In (a1-c1), circle, triangle, and square indicate independent experiments. In this figure, black and blue stand for Sigracet 22bb and PEDOT-PTFE, respectively.
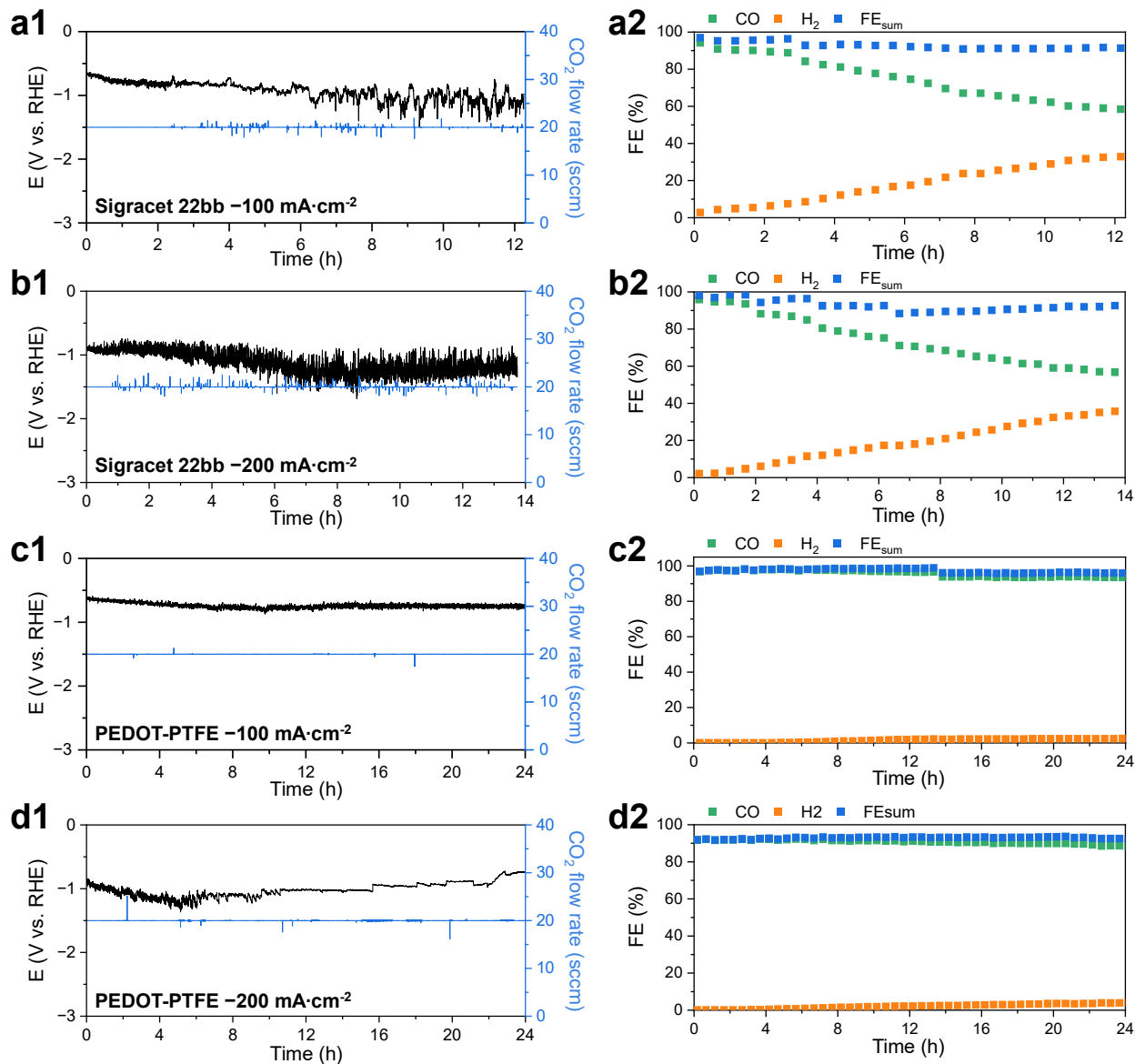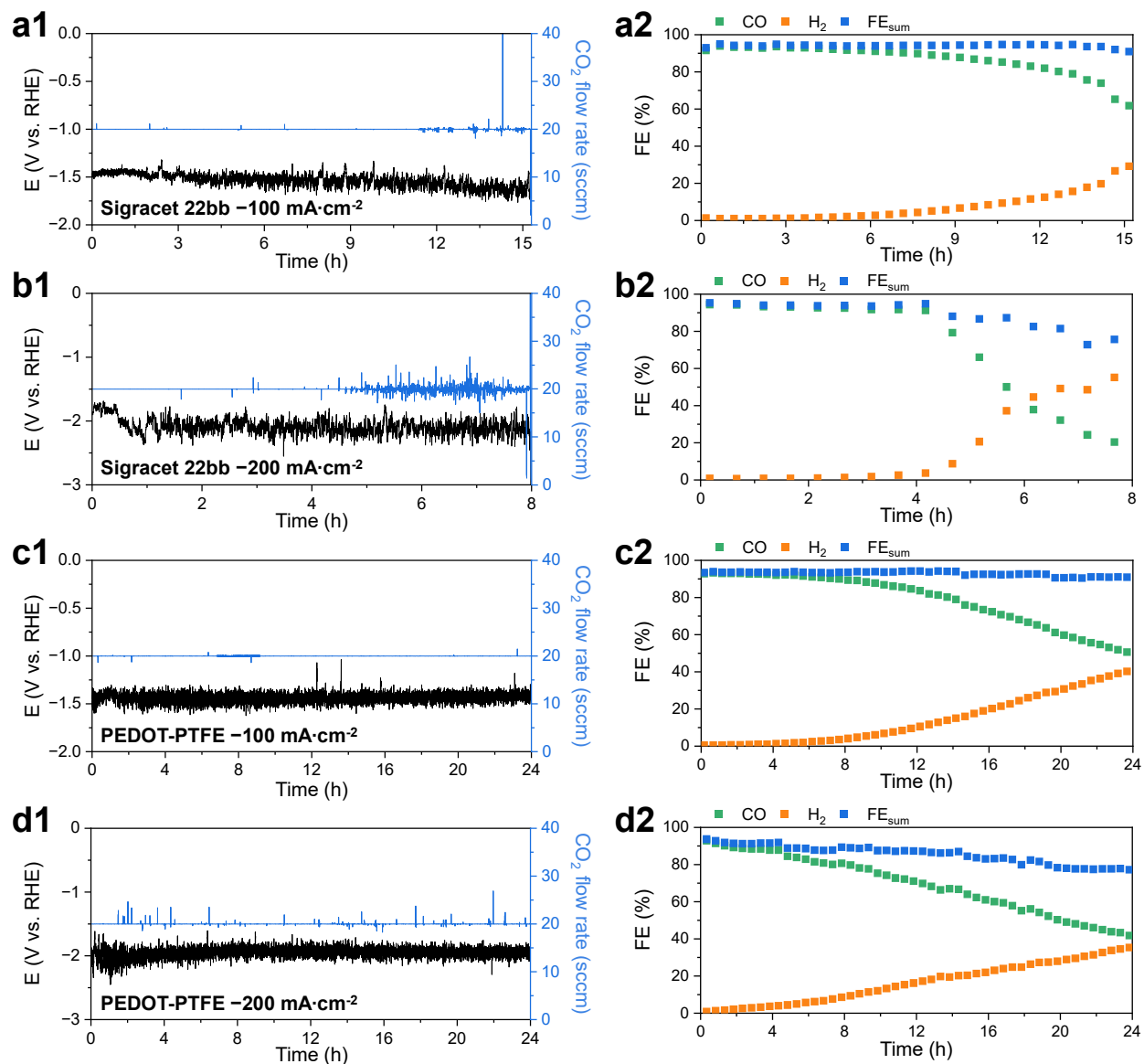
Fig. S14 CO2RR stability test at a constant current density of –100 and –200 mA·cm^{-2} from AgNP 1 mg·cm^{-2} on (a, b) Sigracet 22bb and (c, d) PEDOT-PTFE in 0.8 M KOH. (a1)-(d1) Potential and CO_2 mass flow profile and (a2)-(d2) faradaic efficiency (FE) of CO and H_2 with the sum of FE at constant current. In (a1)-(d1), the black and blue lines represent the recorded potential and CO_2 mass flow rate obtained from the mass flow controller, respectively. In (a2)-(d2), the green, orange, and blue points represent FE_{CO}, FE_{H2}, and sum of FE, respectively.
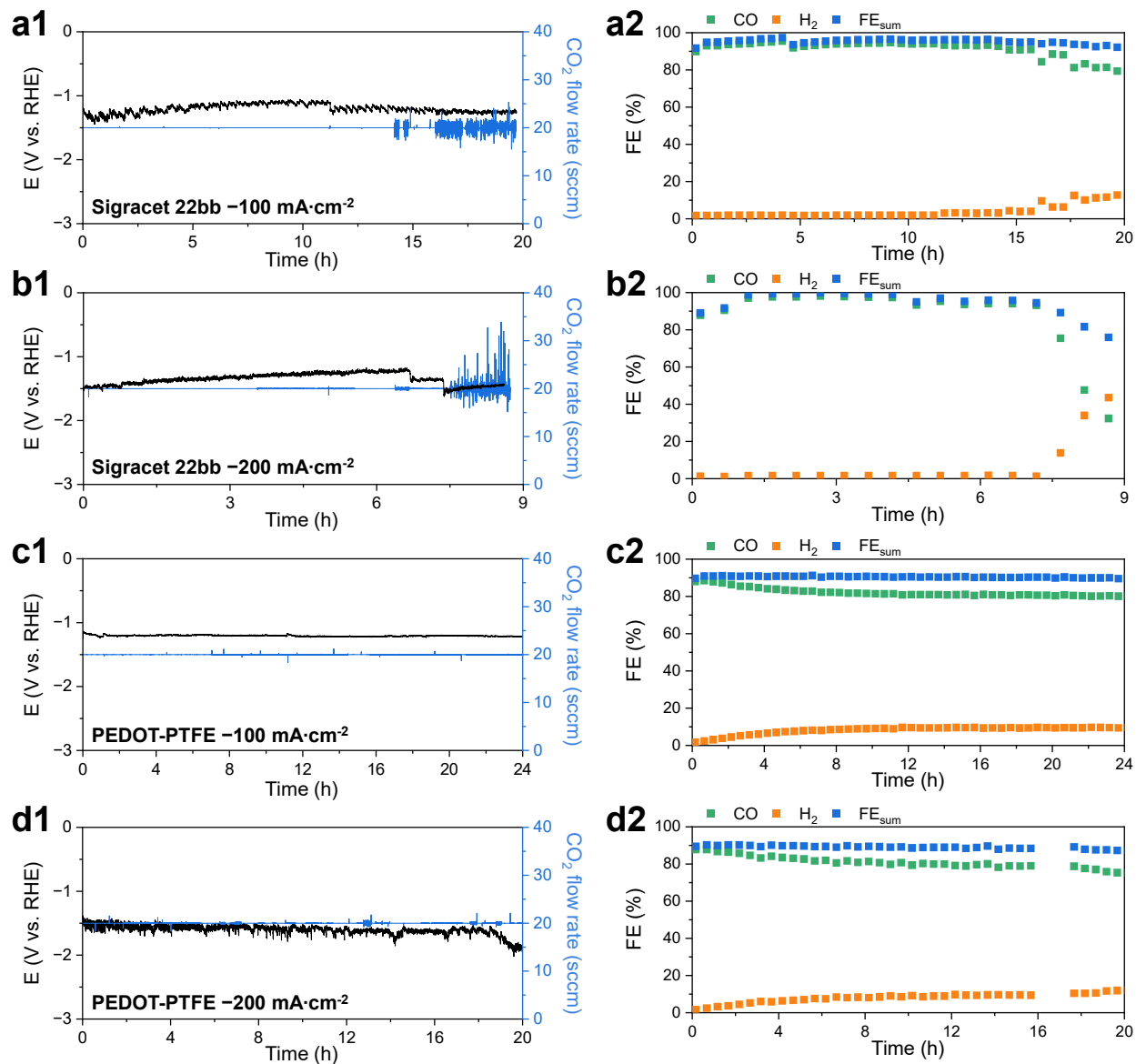
Fig. S15 CO2RR stability test at a constant current density of -100 and -200 mA·cm^{-2} from AgNP 1 mg·cm^{-2} on (a, b) Sigracet 22bb and (c, d) PEDOT-PTFE in 0.8 M KHCO$_3$. (a1)-(d1) Potential and CO$_2$ mass flow profile and (a2)-(d2) faradaic efficiency (FE) of CO and H$_2$ with the sum of FE at constant current. In (a1)-(d1), the black and blue lines represent the recorded potential and CO$_2$ mass flow rate obtained from the mass flow controller, respectively. In (a2)-(d2), the green, orange, and blue points represent FE$_{CO}$, FE$_{H2}$, and sum of FE, respectively.

Fig. S16 CO2RR stability test at a constant current density of –100 and –200 mA·cm^{-2} from AgNP 1 mg·cm^{-2} on (a, b) Sigracet 22bb and (c, d) PEDOT-PTFE in 0.01 M H_2SO_4 with 0.4 M K_2SO_4. (a1)-(d1) Potential and CO_2 mass flow profile and (a2)-(d2) faradaic efficiency (FE) of CO and H_2 with the sum of FE at constant current. In (a1)-(d1), the black and blue lines represent the recorded potential and CO_2 mass flow rate obtained from the mass flow controller, respectively. In (a2)-(d2), the green, orange, and blue points represent FE_{CO}, FE_{H2}, and sum of FE, respectively.
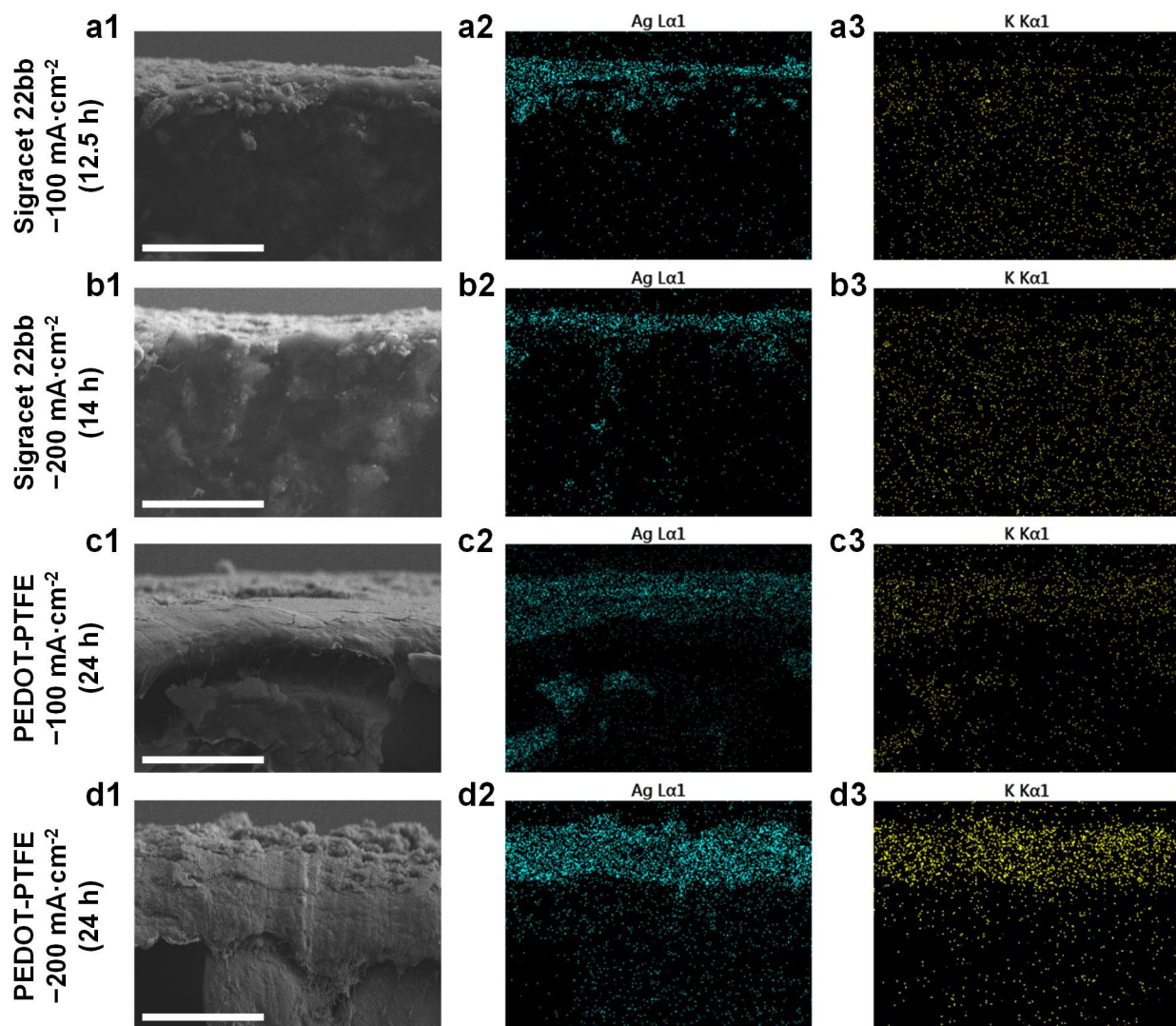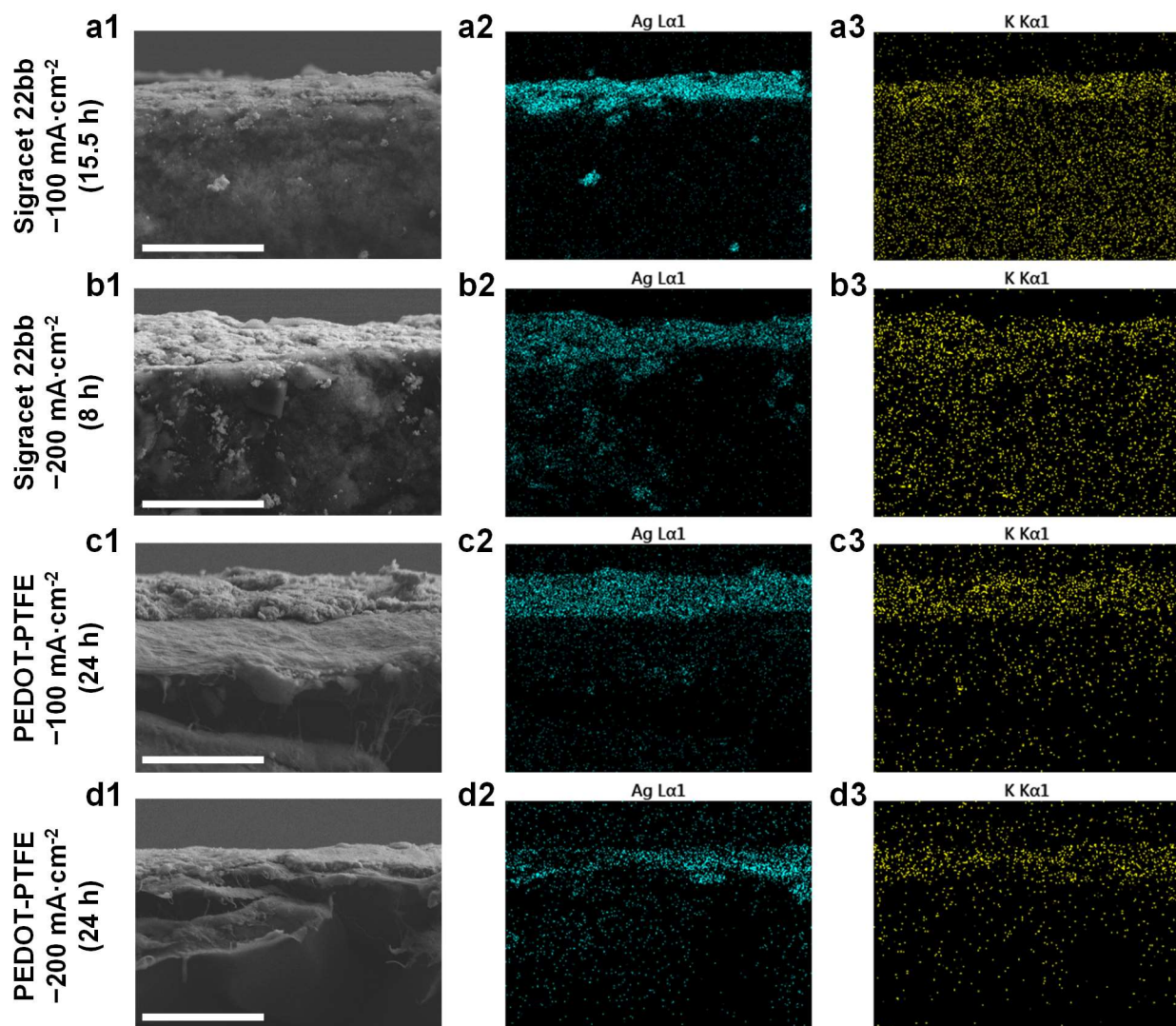
Fig. S17 Cross-section SEM/EDX results of (a, b) Sigracet 22bb and (c, d) PEDOT-PTFE after stability test in the alkaline electrolyte (0.8 M KOH) at (a, c) –100 mA·cm^{-2} and (b, c) –200 mA·cm^{-2}. (a1)-(d1) SEM images and EDX mapping results of (a2)-(d2) Ag and (a3)-(d3) K species. Scale bars indicate 25 μm. For the duration of stability test, (a) 12. 5 h, (b) 14 h, (c) 24 h, and (d) 24 h were used.
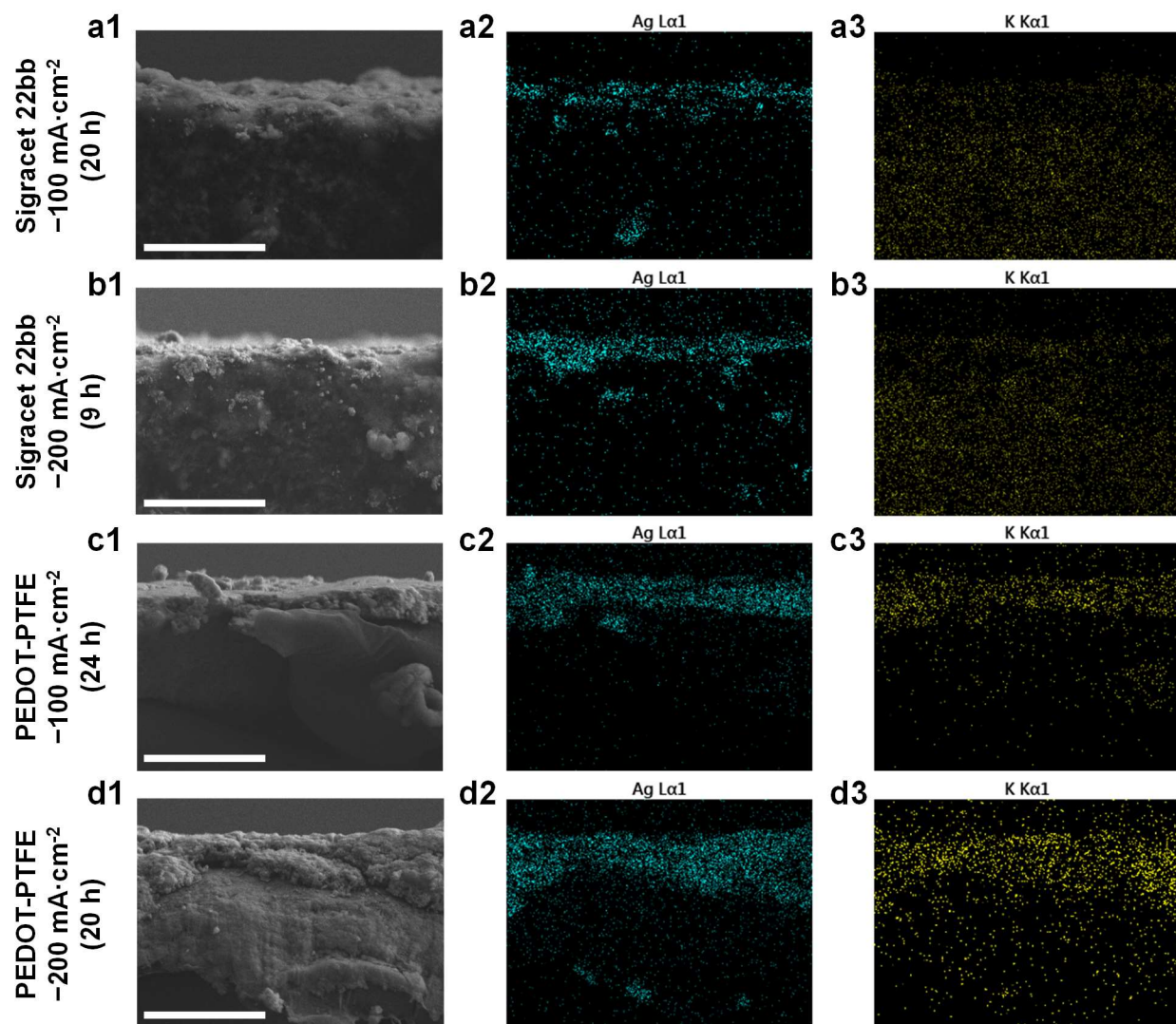
Fig. S18 Cross-section SEM/EDX results of (a, b) Sigracet 22bb and (c, d) PEDOT-PTFE after stability test in the neutral electrolyte (0.8 M $KHCO_3$) at (a, c) –100 mA·cm^{-2} and (b, c) –200 mA·cm^{-2}. (a1)-(d1) SEM images and EDX mapping results of (a2)-(d2) Ag and (a3)-(d3) K species. Scale bars indicate 25 μm. For the duration of stability test, (a) 20 h, (b) 9 h, (c) 24 h, and (d) 20 h were used.
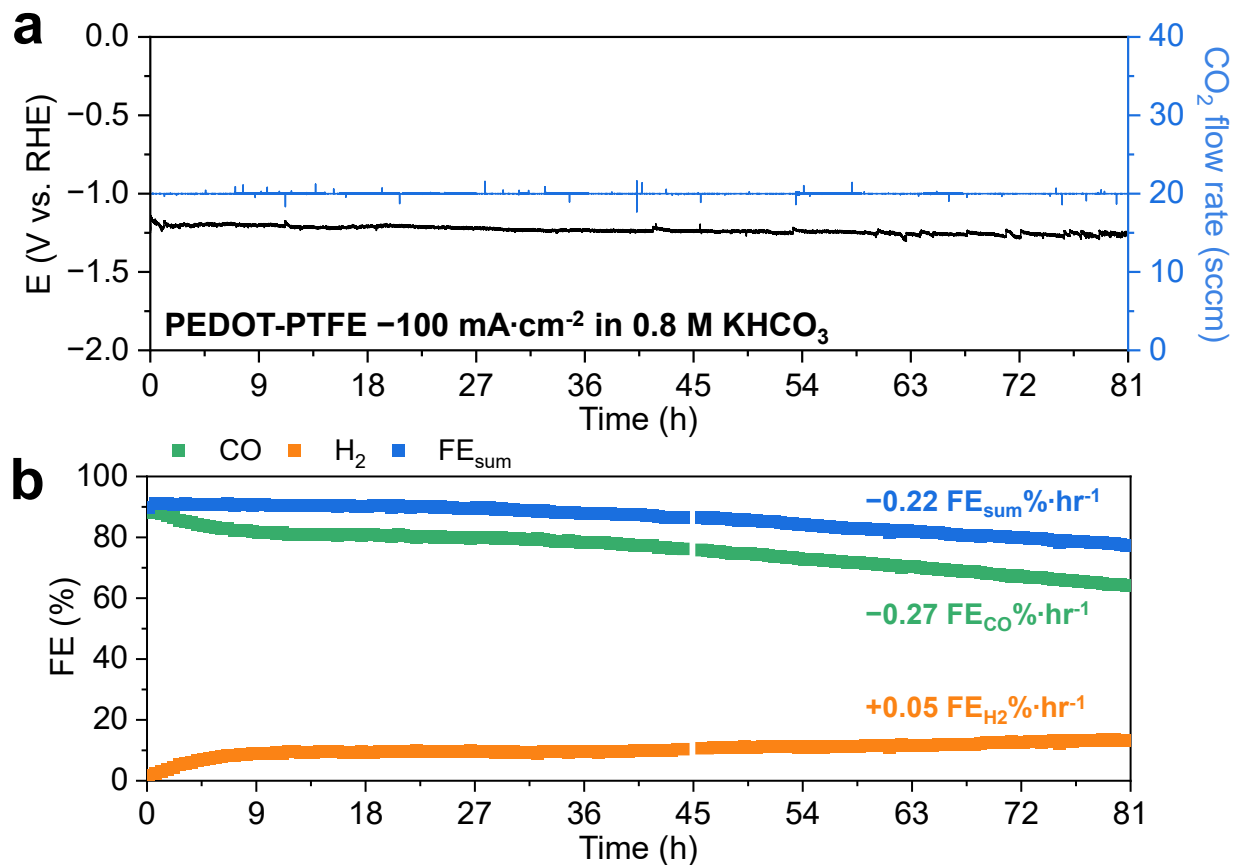
Fig. S19 Cross-section SEM/EDX results of (a, b) Sigracet 22bb and (c, d) PEDOT-PTFE after stability test in the alkaline electrolyte (0.01 M H_2SO_4 with 0.4 M K_2SO_4) at (a, c) –100 mA·cm^{-2} and (b, c) –200 mA·cm^{-2}. (a1)-(d1) SEM images and EDX mapping results of (a2)-(d2) Ag and (a3)-(d3) K species. Scale bars indicate 25 µm. For the duration of stability test, (a) 15.5 h, (b) 8 h, (c) 24 h, and (d) 24 h were used.
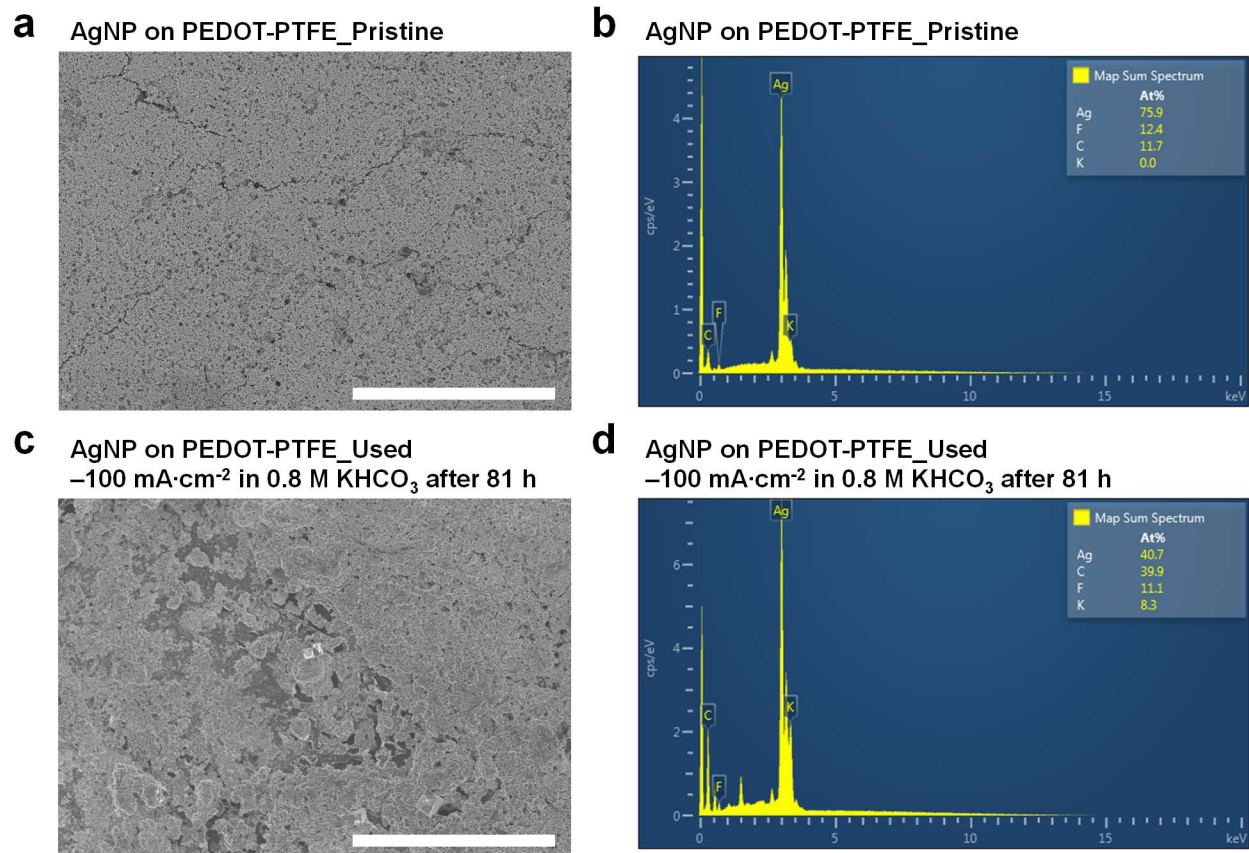
Fig. S20 CO2RR stability test at a constant current density of –100 mA·cm^{-2} from AgNP 1 mg·cm^{-2} on PEDOT-PTFE in 0.8 M KHCO$_3$ for extended period. (a) Potential and CO$_2$ mass flow profile and (b) faradaic efficiency (FE) of CO and H$_2$ with the sum of FE at constant current. In (a), the black and blue lines represent the recorded potential and CO$_2$ mass flow rate obtained from the mass flow controller, respectively. In (b), the green, orange, and blue points represent FE$_{CO}$, FE$_{H2}$, and sum of FE, respectively. After 20 h, the calculated decline rate for FE$_{CO}$, FE$_{H2}$, and FE$_{sum}$ was –0.27, +0.05, and –0.22%·hr^{-1}, respectively.

a AgNP on PEDOT-PTFE_Pristine

b AgNP on PEDOT-PTFE_Pristine

Map Sum Spectrum	At%
Ag	75.9
F	12.4
C	11.7
K	0.0

c AgNP on PEDOT-PTFE_Used
−100 mA·cm^{-2} in 0.8 M KHCO$_3$ after 81 h

d AgNP on PEDOT-PTFE_Used
−100 mA·cm^{-2} in 0.8 M KHCO$_3$ after 81 h

Map Sum Spectrum	At%
Ag	40.7
C	39.9
F	11.1
K	8.3

Fig. S21 (a) SEM image and (b) EDX spectrum of pristine AgNP 1 mg·cm^{-2} on PEDOT-PTFE. (c) SEM image and (d) EDX spectrum of used AgNP 1 mg·cm^{-2} on PEDOT-PTFE after stability test at −100 mA·cm^{-2} in 0.8 M KHCO$_3$ for 81 h. The scale bars in (a) and (c) indicate 50 μm.

Reference

1.   Riley, P. R., Joshi, P., Penchev, H., Narayan, J. & Narayan, R. J. One-Step Formation of Reduced Graphene Oxide from Insulating Polymers Induced by Laser Writing Method. *Crystals* **11**, 1308 (2021).

2.   Schmälzlin, E. *et al.* Raman Imaging with a Fiber-Coupled Multichannel Spectrograph. *Sensors* **14**, 21968–21980 (2014).

3.   Roy, A., Mandal, S. & Menon, R. Lampert triangle formation and relaxation behavior in doped poly(3,4-ethylenedioxythiophene) devices. *Journal of Applied Physics* **129**, 195501 (2021).

4.   Shi, W. *et al.* Micron-thick highly conductive PEDOT films synthesized via self-inhibited polymerization: roles of anions. *NPG Asia Mater* **9**, e405–e405 (2017).

5.   Garreau, S., Louarn, G., Buisson, J. P., Froyer, G. & Lefrant, S. In Situ Spectroelectrochemical Raman Studies of Poly(3,4-ethylenedioxythiophene) (PEDT). *Macromolecules* **32**, 6807–6812 (1999).

6.   Kong, M., Garriga, M., Reparaz, J. S. & Alonso, M. I. Advanced Optical Characterization of PEDOT:PSS by Combining Spectroscopic Ellipsometry and Raman Scattering. *ACS Omega* **7**, 39429–39436 (2022).

7.   Culebras, M., M. Gómez, C. & Cantarero, A. Enhanced thermoelectric performance of PEDOT with different counter-ions optimized by chemical reduction. *Journal of Materials Chemistry A* **2**, 10109–10115 (2014).

8.   Suominen, M., Damlin, P. & Kvarnström, C. Electrolyte effects on formation and properties of PEDOT-graphene oxide composites. *Electrochimica Acta* **307**, 214–223 (2019).

9.   Kvarnström, C. *et al.* In situ spectroelectrochemical characterization of poly(3,4-ethylenedioxythiophene). *Electrochimica Acta* **44**, 2739–2750 (1999).

10.   Pandey, G. P. & Rastogi, A. C. Synthesis and characterization of pulsed polymerized poly(3,4-ethylenedioxythiophene) electrodes for high-performance electrochemical capacitors. *Electrochimica Acta* **87**, 158–168 (2013).

11.   Dzhagan, V. *et al.* Influence of different polymers on photoluminescence of colloidal ZnO nanocrystals. *J Nanopart Res* **24**, 269 (2022).

12.   Gao, T. *et al.* Improving Junction Quality via Modifying the Si Surface to Enhance the Performance of PEDOT:PSS/Si Hybrid Solar Cells. *ACS Appl. Energy Mater.* **4**, 12543–12551 (2021).

13.   Li, S. *et al.* Modifying Reduced Graphene Oxide by Conducting Polymer Through a Hydrothermal Polymerization Method and its Application as Energy Storage Electrodes. *Nanoscale Res Lett* **14**, 226 (2019).

14.   Holze, R. Overoxidation of Intrinsically Conducting Polymers. *Polymers* **14**, 1584 (2022).

15.   Sylvestre, J.-P. *et al.* Surface Chemistry of Gold Nanoparticles Produced by Laser Ablation in Aqueous Media. *J. Phys. Chem. B* **108**, 16864–16869 (2004).

16.   Matolín, V. *et al.* Au+ and Au3+ ions in CeO2 rf-sputtered thin films. *J. Phys. D: Appl. Phys.* **42**, 115301 (2009).

17.   Lanza, G., Martinez Jimenez, M. J., Alvarez, F., Perez-Taborda, J. A. & Avila, A. Valence State Tuning of Gold Nanoparticles in the Dewetting Process: An X-ray Photoelectron Spectroscopy Study. *ACS Omega* **7**, 34521–34527 (2022).

18.   Wilson, M. *et al.* Palladium–poly(ionic liquid) membranes for permselective sonochemical flow catalysis. *Colloids and Surfaces A: Physicochemical and Engineering Aspects* **545**, 78–85 (2018).

19.   Reyes, A. *et al.* Managing Hydration at the Cathode Enables Efficient CO2 Electrolysis at Commercially Relevant Current Densities. *ACS Energy Lett.* **5**, 1612–1618 (2020).

20.   Dinh, C.-T. *et al.* CO2 electroreduction to ethylene via hydroxide-mediated copper catalysis at an abrupt interface. *Science* **360**, 783–787 (2018).